

Dynamic Self-Assembly in Ensembles of Camphor Boats

Siowling Soh, Kyle J. M. Bishop, and Bartosz A. Grzybowski*

Department of Chemical and Biological Engineering and Department of Chemistry Northwestern University, 2145 Sheridan Rd., Evanston, Illinois 60208

Received: November 23, 2007; Revised Manuscript Received: April 10, 2008

Millimeter-sized gel particles loaded with camphor and floating at the interface between water and air generate convective flows around them. These flows give rise to repulsive interparticle interactions, and mediate dynamic self-assembly of nonequilibrium particle formations. When the numbers of particles, N , are small, particle motions are uncorrelated. When, however, N exceeds a threshold value, particles organize into ordered lattices. The nature of hydrodynamic forces underlying these effects and the dynamics of the self-assembling system are modeled numerically using Navier–Stokes equations as well as analytically using scaling arguments.

Dynamic self-assembly (DySA),^{1,2} that is, self-assembly in systems organizing only when dissipating energy, is of fundamental interest in the context of life,^{3–5} and can have practical applications in new classes of smart/adaptive systems and materials.^{6–8} Despite recent progress in the applications of DySA,^{9–11} the study of its underlying principles^{1,12,13} is often hampered by the lack of suitable model systems that would exhibit DySA under well-defined experimental conditions. Here, we describe one such system, in which surface-tension effects give rise to dynamic forces between the components and mediate their DySA into extended patterns (Figure 1). This system is based on the well-known camphor “boats” (i.e., millimeter-sized particles made from agarose and filled with camphor) floating at the interface between water and air. Such particles have been studied extensively by others,^{14–16} mostly for their ability to move autonomously^{15,17} and/or to synchronize their motions in constrained geometries.^{18,19} Although some of these works quantified the nature of the flow-fields around individual particles,^{15,17} they did not investigate whether such flows give rise to interparticle interactions. In the first part of this paper, we show that they indeed do, and that these interactions are repulsive for all separations between the particles. We then demonstrate that the combination of particle–particle repulsions and spatial confinement acting on all particles can lead to their organization into open-lattice structures. Interestingly, for a given area of interface available to the particles, regular patterns emerge only when the number of particles reaches a certain critical value. This “threshold” phase transition, not seen before in artificial DySA systems, is reproduced by a model accounting for interparticle interactions as well as viscous drag acting on the moving particles.

Experimental Section

Disk-shaped gel particles (1 mm in diameter, 500 μm thick) were fabricated as described previously^{20,21} by casting a 5% w/w aqueous solution of agarose against a patterned poly-(dimethylsiloxane) (PDMS) master. The particles were then soaked in a saturated solution of camphor in methanol (1.1 g/mL) for 15 min. Immediately prior to use, the particles were thoroughly rinsed with water to precipitate camphor inside of the particles and, simultaneously, to remove any

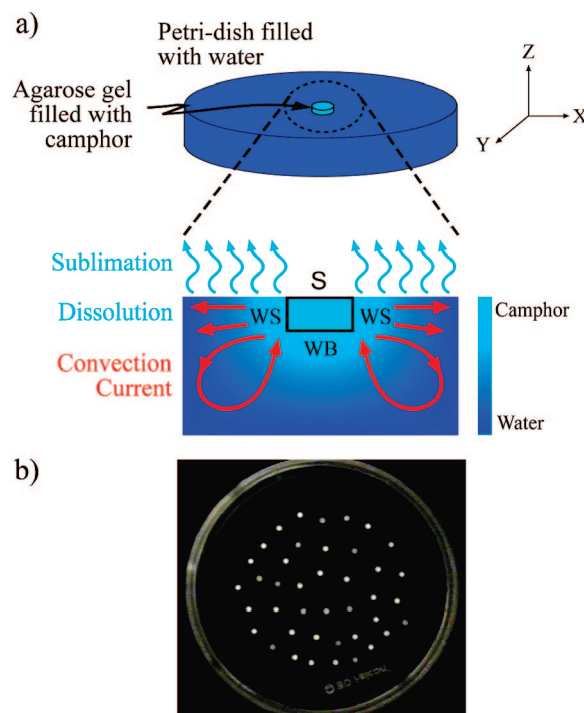


Figure 1. (a) Scheme of a single camphor-soaked, 1 mm agarose disk floating at an interface between water and air. The bottom picture is a side-view of the particle and illustrates the three major processes occurring in the system: camphor transport into the water, convection currents generated by surface tension, and sublimation of camphor at the water–air interface. WB and WS denote the bottom and the side walls of the particle, respectively. (b) An example of dynamically self-assembled array of 41 disks interacting via repulsive hydrodynamic interactions discussed in the text.

excess camphor from the particles' surfaces. This process resulted in a uniform loading of solid camphor microparticles occluded in the gel pieces. Once prepared, the particles were placed at a clean interface between air and water (6.2 mL) in a polystyrene Petri dish (4 cm in diameter). The motions of particles on this interface were recorded by a computer-controlled digital camera. Particle trajectories and/or configurations were analyzed by image recognition software downloaded from <http://physics.georgetown.edu/matlab/>.

* Corresponding author. E-mail: grzybor@northwestern.edu.

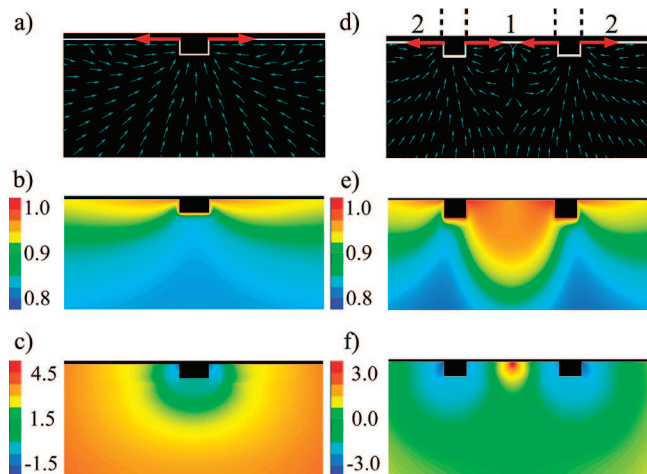


Figure 2. Computational fluid dynamics simulations for an isolated camphor-filled particle (here, approximated as two-dimensional). (a) Velocity flow field around the particle; (b) normalized concentration profile of camphor in water (with respect to the saturation concentration); and (c) the pressure profile (units in Pa). A system of two interacting particles. Graphs show (d) velocity flow field, (e) normalized concentration profile, and (f) pressure profile.

Results and Discussion

1. Flows and Forces between Particles. 1.1. Flows around Isolated Particles. We first discuss the flows generated by an isolated and stationary, camphor-filled particle placed at the interface between water and air (Figure 1a). In doing so, we extend the previous models of the Marangoni convection around camphor boats by accounting for shear stress due to surface tension and sublimation of camphor as boundary conditions on the liquid–air interface. Previous studies¹⁷ have approximated these boundary conditions as volumetric effects occurring only within a thin layer of thickness δ near the interface. This approximation becomes increasingly inaccurate as δ increases. It also does not account for the transport of camphor in the bulk of the fluid which, through Marangoni convection, affects the interfacial camphor concentration and, as we will see later in the text, the forces between camphor-emitting particles.

The system (i.e., particle and the surrounding fluid) is always maintained out of equilibrium by continuous delivery of camphor from the particle onto the interface and by camphor evaporation. The dynamics of this system has three major components: (i) flows generated by gradients of surface tension in the plane of the interface (i.e., Marangoni convection); (ii) camphor transport via both diffusion and convection; and (iii) sublimation of camphor from the liquid–air interface. It is important to note that these processes are mutually related (cf. Figure 1a). For example, gradients in the concentration of camphor at the interface give rise to gradients of surface tension which, ultimately, induce fluid flows. These flows, in turn, alter the distribution of camphor within the fluid and at the interface, and thus influence surface tension gradients that drive the flows.

The fluid flows within the system are governed by the Navier–Stokes equations combined with the continuity equation for an incompressible fluid:

$$\rho \left(\frac{\partial \vec{v}}{\partial t} + \vec{v} \cdot \nabla \vec{v} \right) = -\nabla P + \mu \nabla^2 \vec{v} \quad \text{and} \quad \nabla \cdot \vec{v} = 0 \quad (1)$$

Here, \vec{v} is the fluid velocity, ρ is the density, μ is the viscosity, and P is the pressure. The boundary conditions are such that there is “no slip” both at the walls of the Petri dish and at the fluid–particle interface. At the fluid–air interface, S , camphor-

induced gradients in the surface tension create shearing stresses on the liquid surface. The Cartesian components of these stresses in the plane of the interface (x – y) are related to the gradients of surface tension, γ , by $\vec{\sigma}_{zx} = \partial\gamma/\partial x \vec{e}_x$ and $\vec{\sigma}_{zy} = \partial\gamma/\partial y \vec{e}_y$, where \vec{e}_x and \vec{e}_y are the unit vectors in, respectively, the x and y directions, and the z -axis is normal to S and pointing upward (cf. Figure 1). Because camphor is only sparingly soluble in water and its solute–solute interactions are negligible, the variation of surface tension with concentration can be approximated as linear:²² $\gamma = \gamma_0 - bc$, where γ_0 denotes the surface tension of pure water (72 mN/m), b is a constant of proportionality (henceforth, “shear constant”), and c stands for the concentration of camphor. With this simplification and using the well-known relation between shearing stresses and velocity gradients for a Newtonian fluid, the effects of surface tension to the flow fields can be related by

$$\begin{aligned} \sigma_{zx} &= \mu \left[\frac{\partial v_z}{\partial x} + \frac{\partial v_x}{\partial z} \right]_S = \frac{\partial \gamma}{\partial x} = -b \frac{\partial c}{\partial x} \quad \text{and} \\ \sigma_{zy} &= \mu \left[\frac{\partial v_y}{\partial z} + \frac{\partial v_z}{\partial y} \right]_S = \frac{\partial \gamma}{\partial y} = -b \frac{\partial c}{\partial y} \end{aligned} \quad (2)$$

Next, the equation governing the transport of camphor is

$$\frac{\partial c}{\partial t} + \vec{v} \cdot \nabla c = D \nabla^2 c \quad (3)$$

where D is the diffusion coefficient of camphor in water. For the boundary conditions, there is no flux of camphor through the walls of the dish, $\vec{n} \cdot (D \nabla c - \vec{v} c)_W = 0$ (\vec{n} is the unit vector normal to the walls, and W indicates the lower and side walls of the dish; see Figure 1a). The boundary condition at the liquid/air interface accounting for the flux of camphor due to sublimation can be approximated as¹⁷ $\partial c_S / \partial t = -kc_S$, where k is the rate constant of sublimation and c_S is the camphor concentration at the interface. Because the z -component of velocity in the plane of the interface is zero, the sublimation flux through this interface is equal to diffusive flux of camphor from the fluid’s bulk: $-D \partial c / \partial z|_S = kc_S$. Because of the existence of the so-called Gibbs layer, the surface concentration of camphor, c_S , may be larger than the concentration in the bulk, and can be approximated as^{23,24} $c_S = \alpha c$, where α is the adsorption equilibrium constant. With this approximation, $-D \partial c / \partial z|_S = k' c$, where the apparent evaporation rate $k' = \alpha k$ combines the two unknown parameters.

With these conditions, the equations governing fluid flows were solved numerically using the finite volume method in the “Fluent” CFD modeling suite (by ANSYS, Inc.) with the shear constant, $b = 0.003 \text{ kg} \cdot \text{m}^3 / \text{mol} \cdot \text{s}^2$, and the apparent evaporation rate, $k' = 1 \times 10^{-4} \text{ m/s}$. The value of b was calculated from the $\gamma = \gamma_0 - bc$ relation²⁵ using the experimentally measured surface tension of saturated ($\sim 8 \text{ mM}$ ²⁶) camphor solution, $\sim 50 \text{ mN/m}$. To estimate k' , we first measured (using tracer particles) the fluid velocities ($\sim 1 \text{ mm/s}$) due to convective flows in the plane of the interface and then fitted k' such that the modeled flows reproduced the experimentally observed velocities.

Figure 2a shows a flow field around a particle of rectangular cross-section (approximated as two-dimensional) calculated on the grid of 300 000 finite volume elements.²⁷ This field has two distinct Marangoni convection rolls, with the fluid “sucked” upward from beneath the particles and “ejected” outward with the velocity being highest along the plane of the interface (indicated by the large red arrows in Figure 2a). These features of the flow field agree with previous numerical studies. In addition, our simulations give the corresponding concentration profiles of camphor in the entire fluid (Figure 2b; previous

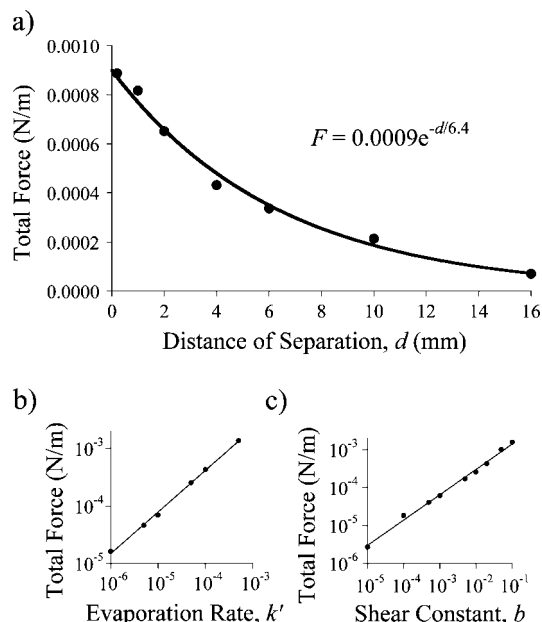


Figure 3. Numerical simulations for the system of two interacting particles show that the repulsive force between particles (a) decreases exponentially with particle separation, (b) increases with increasing rate of camphor evaporation, and (c) increases with increasing shear constant (see the main text for definition).

studies approximated only surface concentrations) and the pressure distribution in the fluid (Figure 2c), both of which are symmetric around the particle's axis of symmetry.

1.2. Flows around and Interactions between Two Proximal Particles. Next, we consider the case of two particles held stationary at a distance, d , from one another. The coupled camphor transport and Navier–Stokes equations are analogous to those described in Section 1.1, but now accounting for boundary conditions on two particle surfaces. When these equations are solved numerically, they yield a velocity flow field and concentration and pressure distributions shown in Figure 2d–f. We observe that these fields/distributions are not symmetric with respect to each particle and are different in the region between the particles (“Region 1”) and outside them (“Region 2”).

The net force on each particle can then be calculated from pressure forces and viscous forces integrated over a particle's surface. Since we are interested only in the horizontal force component, we consider pressure forces acting on the particle's vertical sides and the viscous force acting on the particle's bottom. Integration of pressure distribution on the sidewalls gives the pressure force, $F_p = \int_{WS} p dy$. Likewise, integration of shearing stresses gives the viscous force in the x -direction, $F_s = \int_{WB} \mu (\partial v_x / \partial y) dx$, whose magnitude is significantly smaller than that of F_p , $|F_p/F_s| \sim 300$. Importantly, both of these forces are repulsive for all particle separations, and their sum, F , scales approximately exponentially²⁸ with d , $F = 0.0009e^{-d/6.4}$ N/m (Figure 3a). Also, simulations show that the magnitude of F decreases with decreasing evaporation rate, k , and/or the shear constant, b (Figure 3b,c). The trend shown in Figure 3b agrees with experiments in which the dish was covered with a perforated membrane slowing down the evaporation (i.e., decreasing k).

Qualitatively, the origin of this repulsive force can be explained on the basis of the Bernoulli principle. To show this, we first note that, because both particles emit camphor, its concentration is higher, and the concentration gradients are less

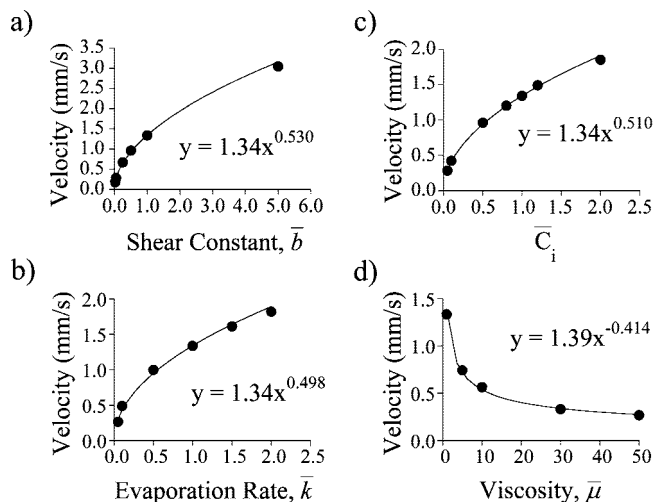


Figure 4. The curves give scaling relationships between characteristic fluid velocity and (a) shear constant, normalized by $b = 0.003 \text{ kg} \cdot \text{m}^3 / \text{mol} \cdot \text{s}^2$, (b) concentration of camphor in agarose gel, normalized by 8 mM saturation concentration at (c), the apparent evaporation rate, normalized by $k' = 1 \times 10^{-4} \text{ m/s}$, and (d) viscosity, normalized by the viscosity of water at 1 mPa·s. Solid markers correspond to numerical simulations performed at a location 10 mm away from the center of a disk (the trends are similar for other locations as well).

steep in Region 1 than in Region 2. Since the shearing stresses, σ_{yx} , acting on the surface of the liquid are proportional to the concentration gradients of camphor (cf. eq 2), they are larger in Region 2 than in Region 1. Consequently, the fluid velocities in Region 2 outside of the particles are greater than those in Region 1 between them. Because the Reynolds numbers in the vicinity of particles are $O(10^2)$, Bernoulli's equation can be used to show that the pressure in Region 1 is higher than that in Region 2. Hence, the particles repel one another.

Finally, we note briefly that qualitative relationships between interparticle forces and other systems parameters can be derived from simple scaling arguments based on the dimensionless Marangoni number, Ma (i.e., the ratio of the capillary stresses driving the convecting fluid to “retarding” viscous stresses). The capillary stress is proportional to the gradient of surface tension, which in turn, is related to the concentration gradient: Capillary stress $\propto (\partial \gamma / \partial x) \propto b(\partial c / \partial x) \propto (bC_0 k) / U$, where U denotes characteristic fluid velocity. On the other hand, the viscous stress is proportional to viscosity and velocity and inversely proportional to the characteristic length scale (here, the particle's radius, R_p): Viscous stress $\propto (\mu U) / R_p$. Therefore, the Marangoni number (Ma) can be written as $Ma = bC_0 k R_p / \mu U^2$ and, provided that the system is in a steady-state, the ratio of the driving and retarding forces must be on the order of unity, $Ma \sim O(1)$. Rearranging, this gives the characteristic velocity, $U \propto (bC_0 k R_p / \mu)^{1/2}$, and pressure, $P = \rho U^2 = \rho b C_0 k R_p / \mu$. Figures 4 and 5 show that these scaling relationships agree with the results of numerical simulations.

1.3. Particle Motions on the Interface. When the particles are not held stationary, they move across the interface. These motions are not only due to the repulsive interparticle interactions, but also due to the inherent ability of the individual particles to propel themselves. This autonomous motion is observed even with high-symmetry particles (e.g., circular disks) and is driven by the fluctuations in the concentration of camphor surrounding the particles. The mechanism of motion has been described in detail in previous papers by Nakata's group.^{15,17–19} Briefly, external disturbances (e.g., air flows above the interface) cause local concentrations of camphor to change. These changes

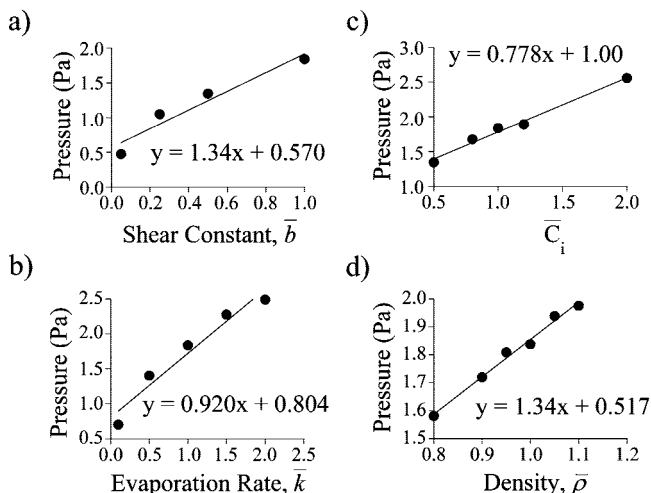


Figure 5. The lines give scaling relationships between characteristic pressure and (a) shear constant, (b) concentration of camphor in agarose gel, (c) apparent evaporation rate of camphor, and (d) fluid density. Normalization factors are the same as in Figure 4. Solid markers correspond to numerical simulations performed at a location 10 mm away from the center of a disk (the trends are similar for other locations as well).

affect the surface tension, which is highest in the regions of lowest concentration. As discussed in Section 1.2, higher surface tension gradients translate into higher shearing stresses on the liquid surface, stronger convection currents, and lower pressure. As a result, the particle starts moving in the direction of lowest concentration. Once in motion, the concentration profile around the particle is no longer uniform, and the particle leaves a trail of camphor *behind* it. This anisotropy in concentration continues to propel the particle in the initial direction until it encounters another source of external disturbance. This disturbance can be another particle or the wall of the container, which also “imparts” a repulsive force on the particle (the pressure is higher between the particle and the proximal wall than in the region of “open” interface). Examples of trajectories of two camphor-filled particles are shown in Figure 6a.

2. Particle Ensembles: From Autonomous Movers to Locked Patterns. **2.1. Characterization of Particle Ensembles.** The behavior of ensembles of camphor-emitting particles depends on how many of such particles populate the interface. When only few particles are present, they move freely, occasionally colliding with one another (cf. Figure 6a). When, however, the number of particles, N , is increased, the particles start moving collectively (Figure 6b) and ultimately “lock” into ordered, patterns (Figure 6c). We studied the transition from free moving to organized assemblies systematically in systems comprising $N = 2$ to $N = 48$ particles confined to a circular interface of radius $R_D = 2$ cm and area $A \sim 12.6$ cm².

For each N , we quantified the behavior of the ensemble in terms of average particle velocity $\langle v \rangle$, and pair distribution function, g (Figure 7a,b). The pair distribution function, $g(r)$, quantifies the likelihood of observing a particular interparticle spacing: for randomly distributed particles, $g(r) = 1$, while for ordered assemblies, $g(r)$ has several peaks at multiples of the lattice spacing. Mathematically, $g(r)$ is defined as in ref 29, $g(r) = (F_C/\rho)\langle\delta(r, r_{ij})\rangle$, where r_{ij} is the distance between particles i and j , $\rho = 2\pi r\Delta r/\pi R_D^2$ is the normalization factor, and F_C is a correction factor to account for the circular boundary of the dish according to ref 30. The discrete delta function is defined as $\delta(r, r_{ij}) = 1$ if $|r - r_{ij}| < \Delta r/2$ and $\delta(r, r_{ij}) = 0$, if $|r - r_{ij}| \geq \Delta r/2$ for a finite “bin-size” Δr (typically, 1 mm). The angular brackets denote the average over both particles and time.

For $N < 7$, the particles move rapidly ($\langle v \rangle \approx 2$ cm/s), their motions are uncorrelated, and there is no spatial order ($g(r) \approx 1$). With the addition of the seventh particle, however, these parameters change dramatically. The particles slow down ($\langle v \rangle \approx 0.06$ cm/s; Figure 7a) and start moving in a synchronized fashion. For $N = 7$, this synchronization is evidenced by the particles moving around the dish as a group (cf. Figure 6b), and a certain degree of internal order is observable with a peak appearing in the $g(r)$ at around $r \approx 8$ mm (Figure 7b). When more particles are added, they start “feeling” the walls of the container (via repulsive forces with the walls, cf. Section 1.3), and the ensemble organizes into an almost ordered lattice. For 48 particles, $\langle v \rangle \approx 0.07$ cm/s, $g(r)$ has a nearest-neighbor peak at ~ 4 mm, and each particle is surrounded by, on average, six neighbors.

As evidenced by the distribution of the white solid particles placed onto the interface (Figure 7c) the array is maintained in this nonequilibrium state by the convection rolls set up by each camphor boat. With the slow evaporation rate used in our experiments, the pattern can persist for times up to 1–2 h before the camphor finally runs out and the structure collapses.

We note briefly that changing the area of the liquid/air interface, A , does influence the “critical” number of particles (here, $N^* = 7$ for $A \sim 12.6$ cm²) at which these particles start to synchronize. In particular, we have observed experimentally that N^* increases with increasing A . The relevant independent variable to capture this effect is the critical number density of camphor particles, $\rho^* = N^*/A$, which, in the limit of “large” areas, should approach a constant value. However, finite-size systems, such as those we investigated here, do not obey this idealized behavior, likely because of boundary effects.

2.1. Modeling of the Particle Ensembles. To reproduce the behavior of particle ensembles and their transition to ordered structures, we implemented a simple model taking into account particles’ autonomous motions, particle–particle and particle–wall repulsions, as well as viscous drag acting on the moving particles. For the system of N particles, this equation in Cartesian coordinates (x, y) with origin (0,0) set at the center of the dish is

$$m \frac{d\vec{v}_i}{dt} = \vec{F}_D (1 - e^{-|\vec{v}_i|/\alpha}) + \left(\sum_{j=1}^N \vec{B} e^{-r_{ij}/\beta} \right) - C \vec{v}_i + \vec{W} e^{-(R_D - \sqrt{x_i^2 + y_i^2})/\lambda} \quad (4)$$

where \vec{v}_i is the velocity of particle i , m is the mass of each particle, R_D is the radius of the interface, α , β , λ , and C are positive constants, and \vec{F}_D , \vec{B} , and \vec{W} are the vectors of, respectively, the driving, particle–particle, and particle–wall forces. The first term on the right-hand side describes the autonomous driving force acting on each particle. To approximate the random motions and occasional halting of particles (as observed experimentally for both isolated particles and for particle collections), this force is assumed stochastic and is turned off for 0.1 s at random times with an average rate of 1 s^{−1}. The reason why this force increases with the particle’s velocity is illustrated qualitatively in Figure 8.^{31,32} An isolated and stationary particle (Figure 8a) has a symmetric concentration profile of camphor around it and thus experiences no net force (neglecting concentration fluctuations, see Section 1.3). When the particle starts moving, concentration gradients of camphor are steeper in front of the particle (as it moves into “clean” water) than at the back (where it constantly leaves a “trail” of camphor); as discussed in Section 1.3, this difference gives rise

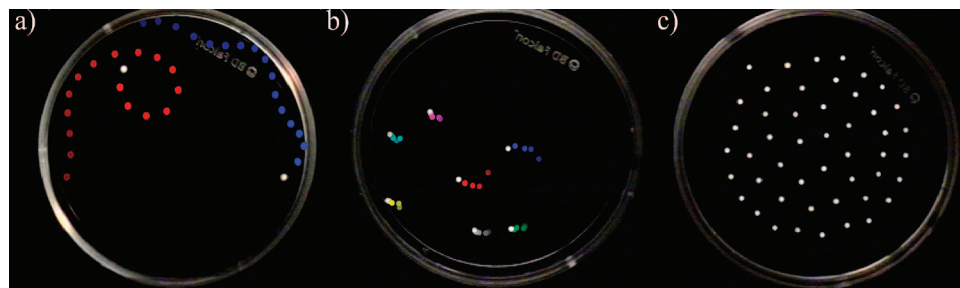


Figure 6. Images of collections of camphor-filled disks (white dots). Colored markers delineate particles' trajectories. (a) Two disks move independently of one another; (b) seven disks move more slowly and in a concerted fashion; (c) 48 disks form a stationary, ordered pattern.

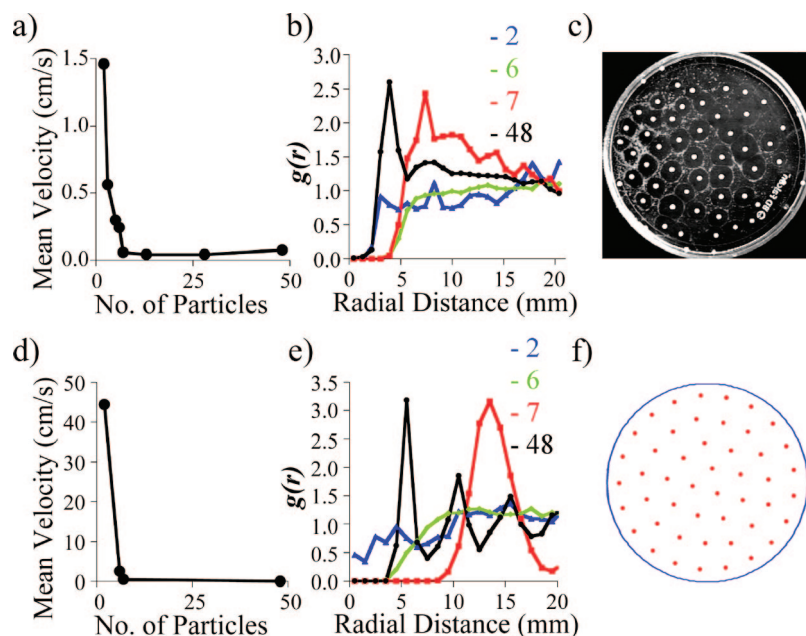


Figure 7. Experimental (a) mean velocities and (b) particle correlation functions for ensembles composed of different numbers of camphor-filled disks. A transition between disordered and ordered assemblies occurs for $N = 7$ particles. (c) Stationary patterns that emerge with large numbers of particles are maintained in steady-state by convection-mediated forces. In this picture, convection rolls are visualized by TiO_2 microparticles sprinkled onto the air/water interface. Calculated (d) mean velocities and (e) particle correlation functions for different values of N are in qualitative agreement with the experimental ones. Simulations were performed with $F_D = 2 \times 10^{-3}/N^2N$ and $\alpha = 0.035$ m/s, and other parameters as described in the main text. (f) An example of a modeled, stationary assembly of 48 particles.

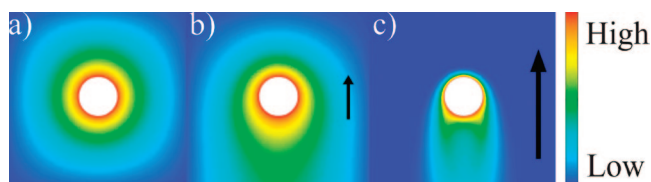


Figure 8. Qualitative concentration profiles of camphor around (a) stationary, (b) slowly moving, and (c) rapidly moving camphor-emitting disks.

to a driving force propelling the particle forward (Figure 8b). As the particle accelerates, the difference in the “front” and “back” gradients and the driving force increase (Figure 8c) until the particle reaches a steady-state velocity (in experiment, ~ 2 cm/s) when the driving force balances the viscous drag force. To account for these effects, we use $\vec{F}_D(1 - \exp(-|\vec{v}|/\alpha))$ such that \vec{F}_D increases with $|\vec{v}|$ monotonically, but the rate of this increase diminishes as the velocity increases and ultimately plateaus. While this formula is only a heuristic approximation, it captures the qualitative features of the experimentally observed particle motions. Also, scaling arguments described in the Supporting Information show that the magnitude of \vec{F}_D decreases with the number of particles as $1/N^2$, which reflects the fact that, with more particles present, more camphor is emitted onto

the interface simultaneously, and the “front”–“back” concentration gradients each particle experiences are shallower. The second term on the right describes the repulsive interparticle forces. These forces decay exponentially with interparticle distance (cf. Section 1.2). In addition, simulations (see Supporting Information) indicate that, while B does not vary appreciably with N , the “range” of interaction, β , depends on the number of particles, N , $\beta \approx 11/N + 1$ (again, this affect is due to more shallow camphor gradients). The third term is the viscous drag force with $C = 6\pi\mu R_P = 1 \times 10^{-5}$ kg/s for a particle approximated as a submerged sphere. The fourth term describes the repulsive force between the particle and the wall of the dish. When a particle approaches the wall, the concentration of camphor builds up in the region between them and leads to a repulsive force similar to that between two particles (but with a smaller range since the wall does not emit camphor; hence $W = B$ and $\lambda = \beta/2$). Finally, the particles are assumed to collide with the walls elastically.

When the equations of motion were solved numerically starting from randomly distributed particles, they reproduced the experimental observations and the transition from free-moving to organized assemblies at $N = 7$ (as evidenced by the abrupt changes in the particle velocities and particle correlation

functions; Figure 7d–f). This agreement suggests that the equations of motions (4) capture the key elements of autonomous particle motions and particle–particle interactions, and can thus be used to model dynamics of other camphor “boat” ensembles.

3. Summary

In conclusion, we described a DySA system in which the flows generated by its components give rise to repulsive hydrodynamic forces that, in turn, lead to the emergence of ordered, out-of-equilibrium structures. The unique feature of this system is the “threshold” transition from free moving to organized assemblies of particles, which is governed by a subtle interplay between the forces agitating/propelling the particles and the repulsive interactions the particles set up between themselves and with the confining boundary. In the wider context, this system adds to the collection of model DySA systems^{7,10,33,34} that not only exhibit DySA under well-defined experimental conditions but are simple enough to study its principles in quantitative detail. Understanding such *general* principles remains a challenging goal for future research on self-assembly in nonequilibrium systems.

Supporting Information Available: Scaling of the driving force with particle number ($F_D \propto 1/N^2$), and the dependence of B on β and N . This material is available free of charge via the Internet at <http://pubs.acs.org>.

References and Notes

- (1) Fialkowski, M.; Bishop, K. J. M.; Klajn, R.; Smoukov, S. K.; Campbell, C. J.; Grzybowski, B. A. *J. Phys. Chem. B* **2006**, *110*, 2482.
- (2) Whitesides, G. M.; Grzybowski, B. *Science* **2002**, *295*, 2418.
- (3) Budrene, E. O.; Berg, H. C. *Nature* **1991**, *349*, 630.
- (4) Jakab, K.; Neagu, A.; Mironov, V.; Markwald, R. R.; Forgacs, G. *Proc. Natl. Acad. Sci. U.S.A.* **2004**, *101*, 2864.
- (5) Parrish, J. K.; Edelstein-Keshet, L. *Science* **1999**, *284*, 99.
- (6) Hartgerink, J. D.; Beniash, E.; Stupp, S. I. *Science* **2001**, *294*, 1684.
- (7) Grzybowski, B. A.; Stone, H. A.; Whitesides, G. M. *Nature* **2000**, *405*, 1033.
- (8) Mirkin, C. A.; Letsinger, R. L.; Mucic, R. C.; Storhoff, J. J. *Nature* **1996**, *382*, 607.

- (9) Campbell, C. J.; Grzybowski, B. A. *Philos. Trans. R. Soc. London, Ser. A: Math. Phys. Eng. Sci.* **2004**, *362*, 1069.
- (10) Grzybowski, B. A.; Radkowski, M.; Campbell, C. J.; Lee, J. N.; Whitesides, G. M. *Appl. Phys. Lett.* **2004**, *84*, 1798.
- (11) Klajn, R.; Bishop, K. J. M.; Grzybowski, B. A. *Proc. Natl. Acad. Sci. U.S.A.* **2007**, *104*, 10305.
- (12) Nicolis, G.; Prigogine, I. *Self-Organization in Nonequilibrium Systems: From Dissipative Structures to Order Through Fluctuations*; Wiley: New York, 1977.
- (13) Groot, S. R.; Mazur, P. *Nonequilibrium Thermodynamics*; Dover Publications: New York, 1984.
- (14) Rayleigh, L. *Proc. R. Soc. London* **1890**, *47*, 364.
- (15) Nakata, S.; Iguchi, Y.; Ose, S.; Kuboyama, M.; Ishii, T.; Yoshikawa, K. *Langmuir* **1997**, *13*, 4454.
- (16) Zhang, J.; Pelton, R. *Langmuir* **1999**, *15*, 8032.
- (17) Kitahata, H.; Hiromatsu, S.; Doi, Y.; Nakata, S.; Islam, M. R. *Phys. Chem. Chem. Phys.* **2004**, *6*, 2409.
- (18) Nakata, S.; Doi, Y.; Kitahata, H. *J. Colloid Interface Sci.* **2004**, *279*, 503.
- (19) Nakata, S.; Hayashima, Y.; Komoto, H. *Phys. Chem. Chem. Phys.* **2000**, *2*, 2395.
- (20) Smoukov, S. K.; Bishop, K. J. M.; Klajn, R.; Campbell, C. J.; Grzybowski, B. A. *Adv. Mater.* **2005**, *17*, 1361.
- (21) Campbell, C. J.; Baker, E.; Fialkowski, M.; Grzybowski, B. A. *Appl. Phys. Lett.* **2004**, *85*, 1871.
- (22) Adamson, A. W.; Gast, A. P. *Physical Chemistry of Surfaces*, 6th ed.; Wiley: New York, 1997.
- (23) Brian, P. L. T. *AIChE J.* **1971**, *17*, 765.
- (24) Bragard, J.; Slavtchev, S. G.; Lebon, G. *J. Colloid Interface Sci.* **1994**, *168*, 402.
- (25) Kang, K. H.; Choi, C. K.; Hwang, I. G. *AIChE J.* **2000**, *46*, 15.
- (26) *The Merck Index*, 14th ed.; Merck: Whitehouse Station, NJ, 2006.
- (27) To achieve convergence, even the 2D simulations required the use of ca. 300 000 volume elements. Full 3D simulations were computationally prohibitive with our current computational/software resources.
- (28) Thomas, H.; Morfill, G. E.; Demmel, V.; Goree, J.; Feuerbacher, B.; Mohlmann, D. *Phys. Rev. Lett.* **1994**, *73*, 652.
- (29) Allen, M. P.; Tildesley, D. J. *Computer Simulation of Liquids*; Oxford University Press: New York, 1987.
- (30) Bell, R. J. *Nature* **1969**, *221*, 50.
- (31) Nagayama, M.; Nakata, S.; Doi, Y.; Hayashima, Y. *Physica D* **2004**, *194*, 151.
- (32) Kitahata, H.; Yoshikawa, K. *Physica D* **2005**, *205*, 283.
- (33) Ng, J. M. K.; Fuerstman, M. J.; Grzybowski, B. A.; Stone, H. A.; Whitesides, G. M. *J. Am. Chem. Soc.* **2003**, *125*, 7948.
- (34) Grzybowski, B. A.; Stone, H. A.; Whitesides, G. M. *Proc. Natl. Acad. Sci. U.S.A.* **2002**, *99*, 4147.

JP7111457